

FORTGESCHRITTENEN PRAKTIKUM II

Optical pumping

11.04.2016

Benjamin Winkelmann
Peter Spalthoff

Tutor: Dominik Schomas

1 Abstract

Optical pumping between Zeeman states of rubidium isotopes ^{87}Rb and ^{85}Rb that are split up by well controlled magnetic fields allows for the precise calculation of the earths magnetic field, hyperfine constants A of the two isotopes as well as the relaxation time of the polarized states. The resulting hyperfine constants were calculated as

$$A_{2S_{1/2}}(^{87}\text{Rb}) = (14.61 \pm 0.13) \mu\text{eV} \quad (1.1)$$

$$A_{2S_{1/2}}(^{85}\text{Rb}) = (4.50 \pm 0.08) \mu\text{eV} \quad (1.2)$$

$$A_{2P_{1/2}}(^{87}\text{Rb}) = (1.52 \pm 0.18) \mu\text{eV} \quad (1.3)$$

The hyperfine constant $A_{2P_{1/2}}(^{85}\text{Rb})$ could not be calculated since the relevant peaks could not be separated with the set-up. The earths' magnetic field components were calculated to be

$$B_v = (37.1 \pm 1.4) \mu\text{T} \quad (1.4)$$

$$B_h = (2.36 \pm 0.21) \mu\text{T} \quad (1.5)$$

Of the two methods used to calculate the relaxation times, only the Dehmelt method produced a reasonable result for the relaxation time:

$$T_R = (4.8 \pm 1.5) \text{ ms} \quad (1.6)$$

Contents

1 Abstract	1
List of Figures	III
List of Tables	IV
2 Physical principles	1
2.1 Hyperfine structure and Zeeman splitting	1
2.2 Optical pumping	3
2.3 Relaxation processes	4
2.4 Larmor precession of the spin	5
3 Experimental set-up	6
4 Characterization of the laser diode	7
5 Spectroscopy of the hyperfine structure	8
5.1 Set-up and procedure	8
5.2 Data analysis	9

6 Double resonance	13
6.1 Set-up and procedure	13
6.2 Data analysis	14
6.3 Discussion	17
7 Spin precession	18
7.1 Set-up and procedure	18
7.2 Analysis	19
8 Relaxation measurements - Dehmelt method	22
8.1 Set-up and procedure	22
8.2 Data Analysis	22
9 Relaxation measurements - Franzen method	25
9.1 Set-up and procedure	25
9.2 Data Analysis	25
10 References	29

List of Figures

2.1	Hyperfine structure of Rubidium	2
2.2	Hyperfine structure energies	3
2.3	Optical pumping	4
3.1	Basic experimental set-up	6
4.1	Characteristic curve of the laser diode	7
5.1	Experimental set-up for the Calibration	8
5.2	Bend in modulating current	9
5.3	Etolon peaks	10
5.4	Lienear fit on etalon peak positions	11
5.5	The HFS-spectrum	12
6.1	Double resonance set-up	14
6.2	Double resonance peaks	15
7.1	Spin precession set-up	18
7.2	Example spin precession	19
7.3	Linear fit on precession frequencies	20
8.1	Set-up relaxation measurements - Dehmelt	22
8.2	Example of Dehmelt relaxation	24
8.3	Fit on the inverse orientation times	25
9.1	Set-up relaxation measurements - Franzen	26
9.2	Example of Franzen relaxation	27
9.3	Relaxation time fit Franzen	28
9.4	Chopper signal 1.5V	29

List of Tables

5.1	HFS peaks fit results	13
6.1	Properties of the magnetic field coils	15
6.2	Results of the double resonance measurements	16
7.1	Properties of the magnetic field coils	21
8.1	Relative intensities of the filters	23

2 Physical principles

2.1 Hyperfine structure and Zeeman splitting

This section is based on the detailed elaborations in [1].

The fine structure levels of the atomic spectrum, which splits the basic levels into sub-levels due to spin-orbit interaction, can be shown to be split into even finer levels, whose energetic distances are roughly three orders of magnitude smaller than those of the fine structure. This is called the 'hyperfine structure' and is mainly caused by the interaction of the nuclear magnetic dipole and quadrupole moment and the magnetic field of the shell electrons. Its structure for the two Rubidium isotopes that are used in this experiment can be seen in figure 2.1.

As the nucleus is charged and, expressed as the nuclear spin \vec{I} , has angular momentum, it also has a magnetic moment, which is $\vec{\mu}_I = \frac{g_I \mu_K}{\hbar} \vec{I}$, where g_I is the g-factor of the nucleus and μ_K is the nuclear magneton.

With the total angular momentum of the electrons \vec{J} , the total angular momentum of the atom can be written as

$$\vec{F} = \vec{J} + \vec{I}, \quad |I - J| \leq F \leq I + J \quad (2.1)$$

The energy difference between hyperfine structure levels can then be shown to be

$$\Delta E_{HFS} = -\vec{\mu}_I \cdot \vec{B}_J = \frac{A}{2}(F(F+1) - J(J+1) - I(I+1)) \quad (2.2)$$

where $A = \frac{g_I \mu_K B_J}{\sqrt{J(J+1)}}$ is the hyperfine constant. Neighboring levels thus have an energy difference of

$$\Delta E_{HFS}(F+1) - \Delta E_{HFS}(F) = A(F+1) \quad (2.3)$$

This structure for the rubidium isotopes used in this experiment can be seen in figure 2.2.

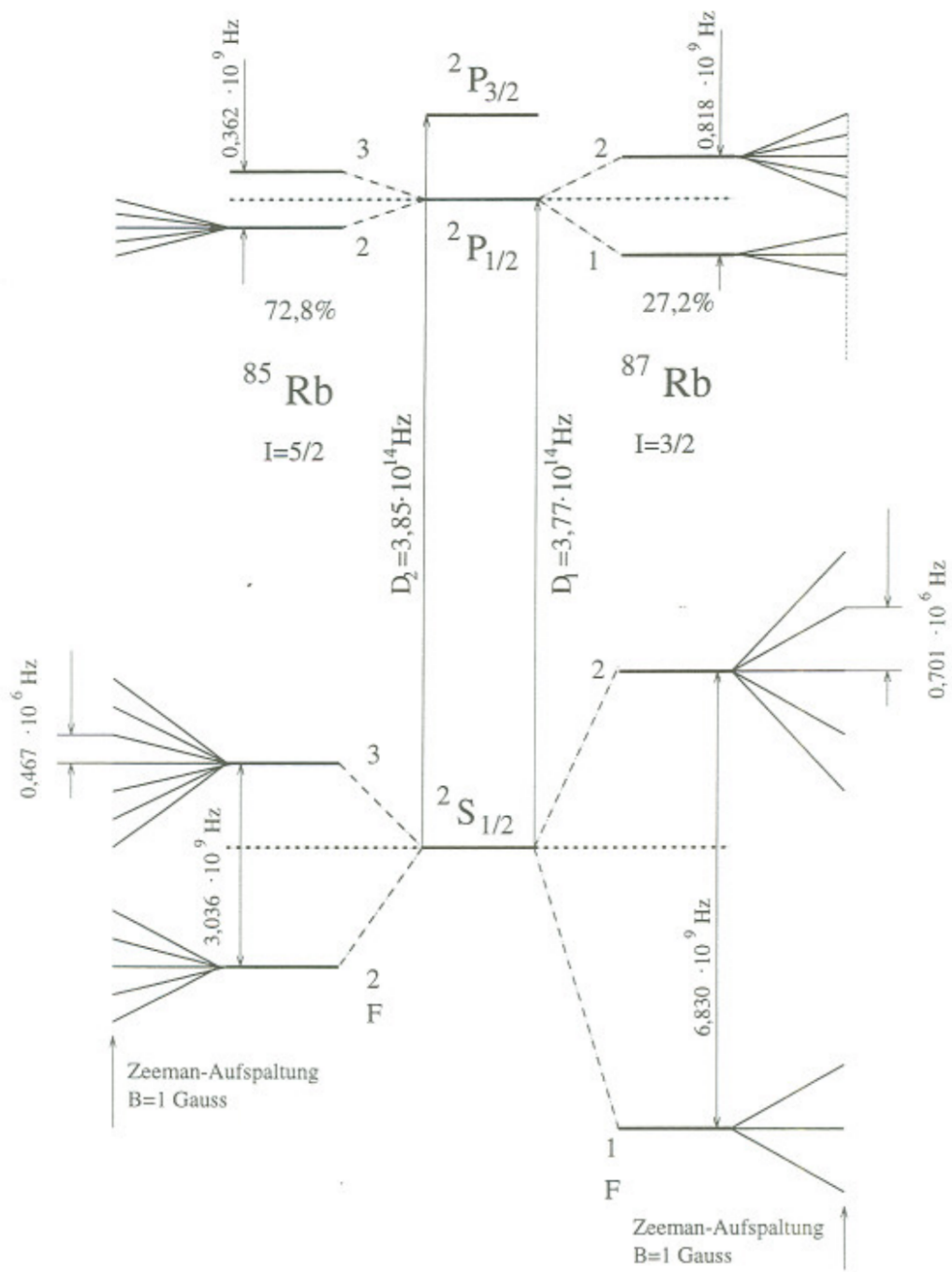


Figure 2.1: The hyperfine structure of the two isotopes of Rubidium used in the experiment. The hyperfine levels in turn are split due to the Zeeman effect caused by an external field of $B = 1 \text{ G}$. [1]

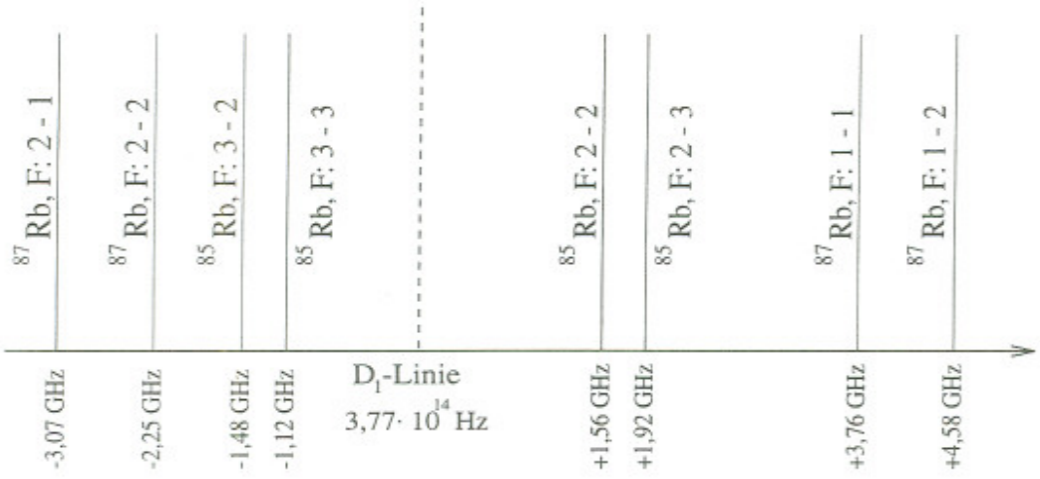


Figure 2.2: Energies of a set of hyperfine levels of the two isotopes used in the experiment. [1]

These hyperfine levels can in turn be split into $2(F + 1)$ sub-levels in the presence of an external magnetic field. The according quantum number is $-F \leq m_F \leq F$. As long as the magnetic field is weaker than the spin-orbit coupling or, in other terms, $g_J\mu_B B_0 \ll A$, this is called the Zeeman effect. The effect for larger fields, where the spin-orbit coupling is disrupted, is called Paschen-Back effect.

For the Zeeman effect, the energy difference of the levels is

$$\Delta E_{\text{Zeeman}} = \frac{g_J}{2(I + \frac{1}{2})} \mu_B B_0 \quad (2.4)$$

where μ_B is the Bohr magneton.

2.2 Optical pumping

In general, pumping refers to constantly transferring electrons into higher energy levels until significantly more electrons are in the higher than in the lower state. This is called population inversion.

In the case of this experiment, this is done using a laser diode. As the goal is to examine magnetic fields using the Zeeman splitting, a way must be found to create population inversion within a single non-degenerate hyperfine structure level. Normally, electrons are equally distributed between said levels.

The selection rules for transitions

$$\begin{aligned} \Delta F &= 0, \pm 1 & (F = 0 \leftrightarrow F = 0) \\ \Delta m_F &= 0, \pm 1 \end{aligned} \quad (2.5)$$

allow for a convenient way to change that. If only σ^+ -polarized light is used, only transitions with $\Delta m_F = +1$ are caused. Since the following decay is random within the

bounds of the transition rules, the laser will pump all electrons into the $^2S_{1/2}$ state with $m_F = +2$, $F = 2$ for ^{87}Rb and $m_F = +3$, $F = 3$ for ^{85}Rb . Figure 2.3 illustrates this for two exemplary transitions.

Mathematically, this process can be described as

$$\left(\frac{dn}{dt} \right)_P = \frac{N - n}{T_P} \quad (2.6)$$

where n is difference of the levels in the two-level system, N the overall number of atoms in the system and T_P the characteristic pumping time of the system.

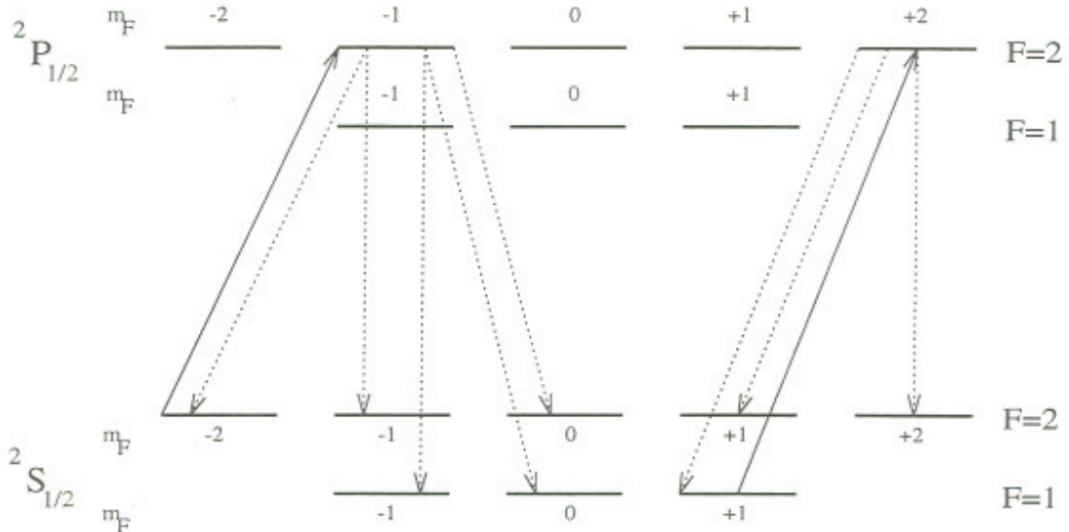


Figure 2.3: Optical pumping for ^{87}Rb . The σ^+ polarized light can only cause transitions with $\Delta m_F = +1$, thus achieving the desired pumping effect.

2.3 Relaxation processes

The desired pumping effect is counteracted mainly by three relaxation effects:

Diffusion to the wall: Upon hitting the glass containment, the rubidium atoms may lose their polarization. This process is inhibited by a buffer gas, which limits the mean free path of the atoms.

Collisions with the buffer gas: The rubidium atoms may use their polarization due to collisions with the buffer gas. The cross section of this event depend highly on what kind of gas is used. Best results are achieved with noble gases - in the case of this experiment, krypton was used.

Spin exchange When rubidium atoms collide, they may interchange their spins. While the overall polarization is preserved, the decoupling of nuclear and electron spins lead to a faster relaxation time. Much more detailed elaborations can be found in [3].

Overall, the relaxation can be described by the following differential equation

$$\left(\frac{dn}{dt} \right)_R = -\frac{n}{T_R} \quad (2.7)$$

where T_R is the characteristic relaxation time. A value of $T_R^{theo} = 6.5$ ms is given in [1]. The overall process of polarization orientation is thus the sum of equations 2.6 and 2.7:

$$\left(\frac{dn}{dt} \right)_O = \left(\frac{dn}{dt} \right)_P + \left(\frac{dn}{dt} \right)_R = \frac{N}{T_P} - n \left(\frac{1}{T_P} + \frac{1}{T_R} \right) \quad (2.8)$$

The solution of this equation is an exponential

$$n(t) \propto e^{-\frac{t}{\tau}} \quad (2.9)$$

where

$$\tau = \frac{1}{T_P} + \frac{1}{T_R} \quad (2.10)$$

2.4 Larmor precession of the spin

If the ensemble is polarized along a certain magnetic field and one component of said field is suddenly set to zero, the polarization precesses around the remaining field. The precession frequency is

$$f_L = \frac{g_F \mu_B}{h} \cdot B =: \alpha \cdot B \quad (2.11)$$

where g_F are the Landé factors for the rubidium isotopes, quantified by Baur [1] as $g_F(^{85}Rb) = 1/3$ and $g_F(^{87}Rb) = 1/2$. The proportionality constant between the frequency and the remaining magnetic field thus is

$$\alpha(^{85}Rb) = 4.665 \text{ kHz}/\mu\text{T} \quad \alpha(^{87}Rb) = 6.998 \text{ kHz}/\mu\text{T} \quad (2.12)$$

3 Experimental set-up

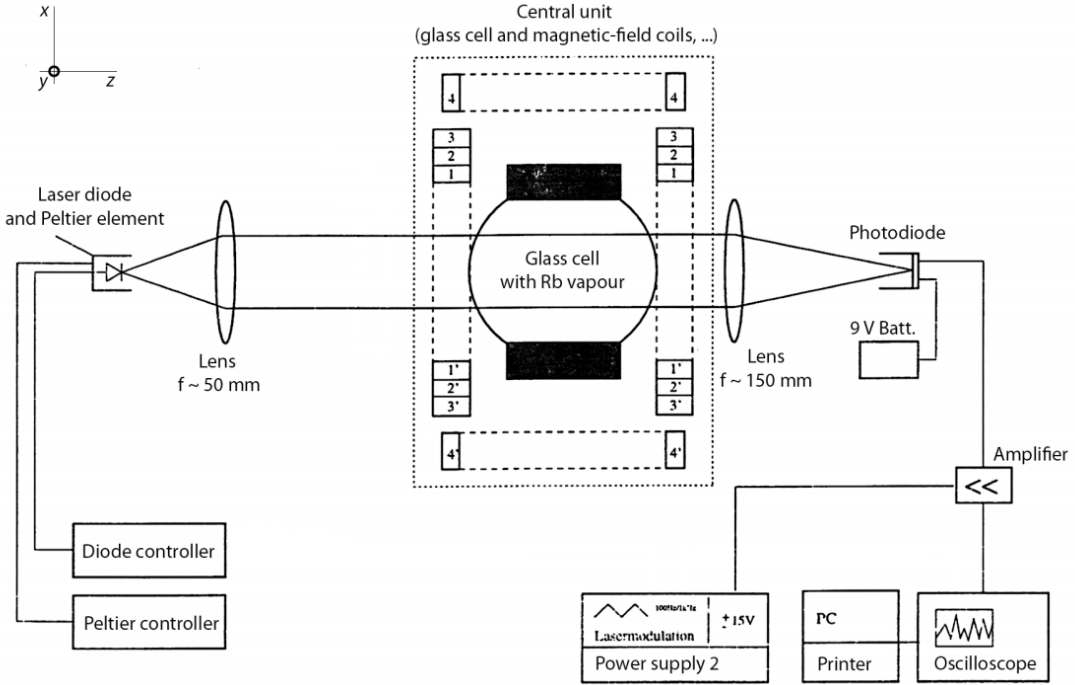


Figure 3.1: Basic set-up of the experiment. For the various tasks, parts can be placed onto the optical bench. The glass cell can be removed from the central unit. [2] (modified)

At the core of the experimental set-up is the glass cell with the Rubidium vapor and the buffer gas. It can be taken in and out of the central unit, which in turn houses four sets of Helmholtz coils. Another such pair is directly attached to the casing of the glass cell, along with a radio frequency generator and an appropriate frequency measuring device.

A laser diode provides coherent light in the energy range needed to pump the desired hyperfine state of the Rubidium atoms in the glass cell. Laser diodes send out linearly polarized light with a small spectral width. Frequency and intensity vary with the temperature of the diode as well as the current running through it, which is why the diode is kept at constant temperature using a Peltier element. For the diode to start emitting light, a certain current threshold has to be reached. From then on, the intensity depends linearly on the current if temperature is kept constant. However, mode jumps occur when the number of standing waves in the resonator changes and measurements need to be taken in areas that do not include such jumps.

The beam is collimated by a lens before passing through other optical elements and,

after passing through the central unit, is refocused onto a photo-diode. This can be seen in figure 3.1. The output of the diode is amplified and can then be observed on an oscilloscope, which in turn can be read out by a computer to produce analyzable data.

The set-up varies greatly from one part of the experiment to another and will thus be explained in detail in the appropriate sections.

4 Characterization of the laser diode

For later measurements, it is important to determine the range of supply current in which the diodes intensity increases linearly without mode jumps occurring. The gas cell is taken out of the central unit for this part of the experiment.

After turning on the peltier element, a few minutes should pass before measurements are started to allow the diode to thermalize. Measurements were taken at $T = 34.3^\circ$.

Since the photo diode saturated for laser diode currents upwards of $I_L = 65$ mA, a neutral filter (D2,6, see figure ??) is used to limit intensity so that the photo diode barely does not reach saturation.

The intensity of the diode is now measured at supply currents between 0 – 90 mA. The results can be seen in figure 4.1. The threshold current is roughly 51.6 mA, followed by the linear domain until mode jump occur at around 72 mA to 82 mA.

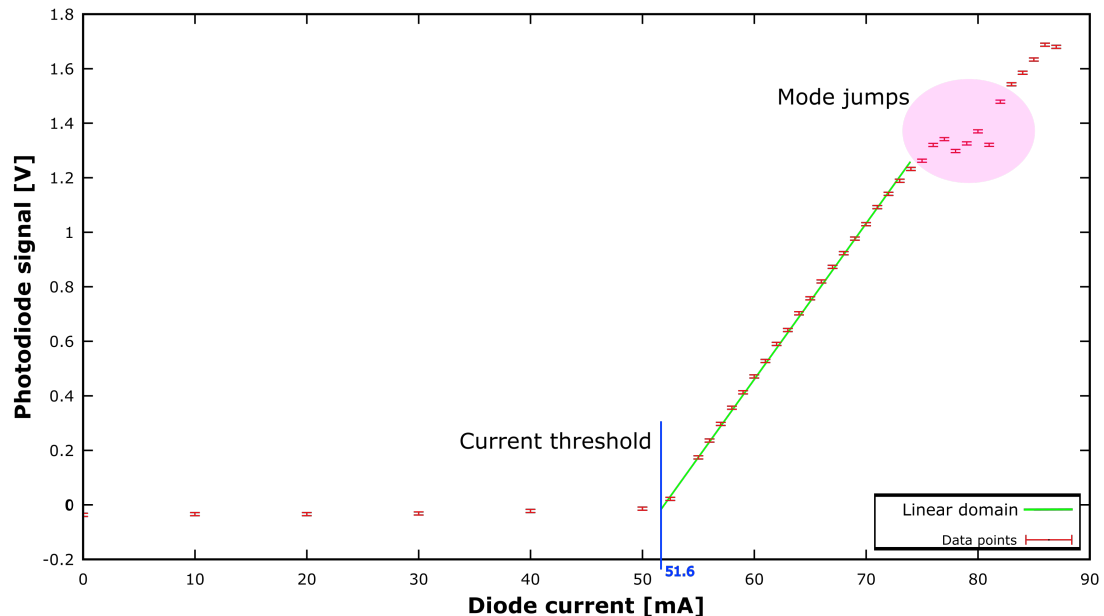


Figure 4.1: The characteristic curve of the laser diode for supply currents up to 90 mA. A mode jump can clearly be seen in the upper right corner.

5 Spectroscopy of the hyperfine structure

5.1 Set-up and procedure

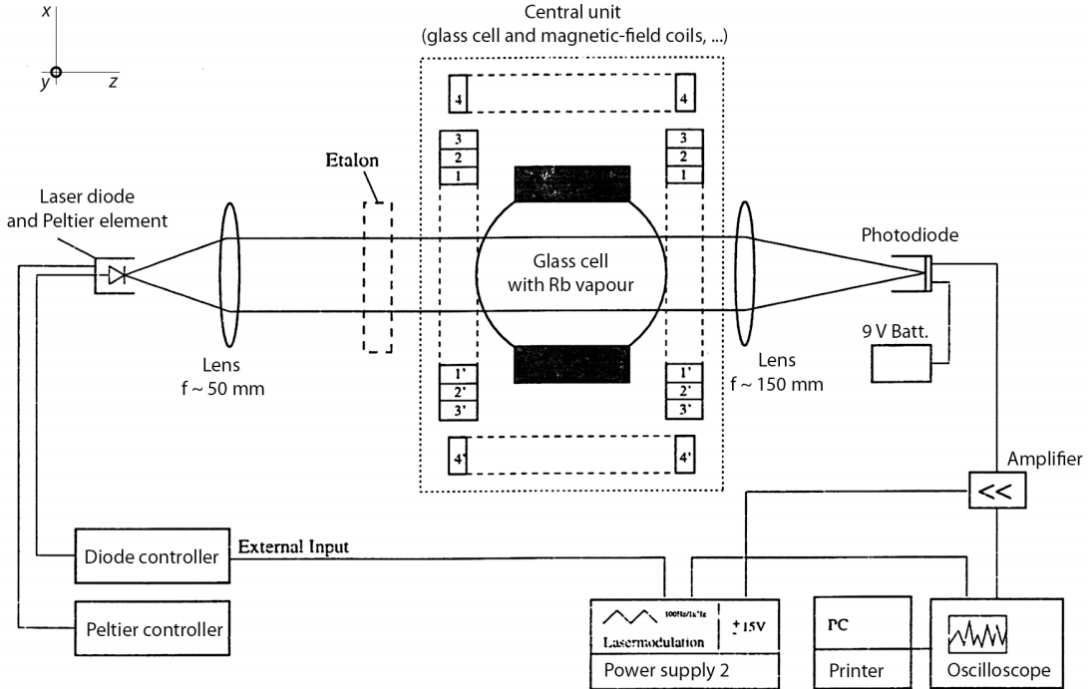


Figure 5.1: Experimental set-up for the calibration measurements. An etalon is placed after the left lens and can be removed for the HFS-spectrum measurement.[2]

Laser scan-rate

A Fabry-Pérot-Interferometer (etalon), which is a set of parallel, almost completely reflecting surfaces facing each other, is used to gauge the diode. The intensity at the photo diode will be drastically damped unless the laser wavelength allows for constructive interference to occur between the surfaces. The wavelengths at which light passes the interferometer are thus equidistant.

The diode current is then modified with a saw-tooth voltage, which is also used to trigger the oscilloscope (see figure 5.1). It is important to measure the scan-rate in a range of diode currents where the intensity response is linear and where the HFS-spectrum is actually visible (see next section). To get a solid calibration, at the very least 3 etalon peaks are necessary. These two factors have to be taken into consideration when choosing the measurement interval.

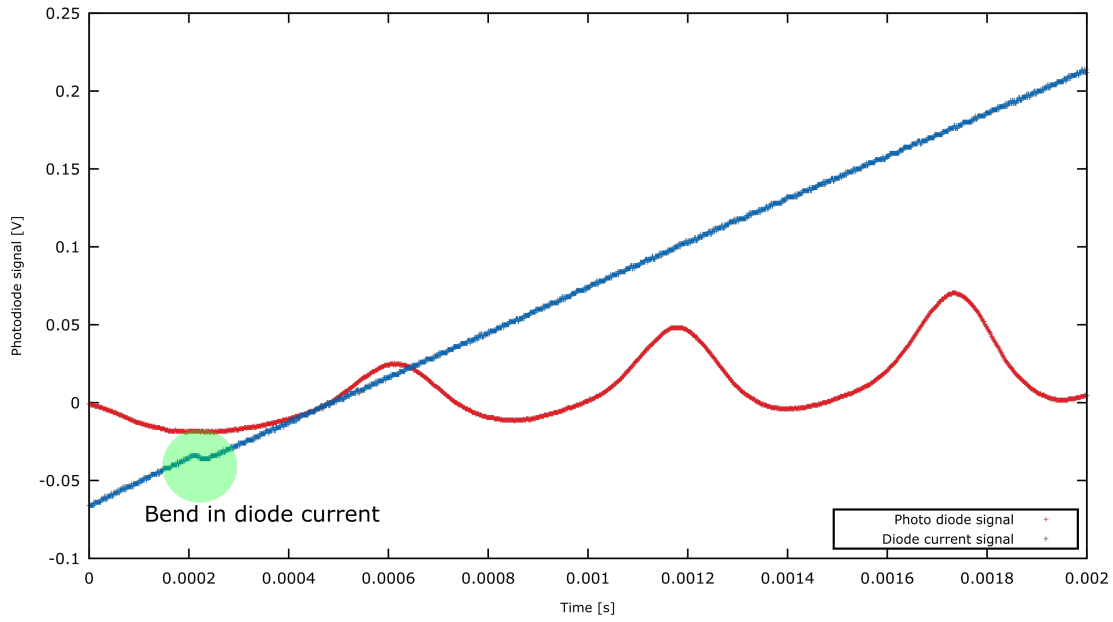


Figure 5.2: In the bottom left corner, a clear bent in the diode current can be seen. These measurements were not used, a better current range was chosen instead.

Figure 5.2 shows a bend in the diode current. Such areas need to be avoided when taking measurements, as they would lead to non-equidistant peaks in the etalon spectrum and unnecessarily complicate data analysis. The base current for the measurements was $I_L = (58.5 \pm 0.1)$ mA, where the uncertainty is the digit error of the multimeter ELTELEC, for which no data sheet was available. The temperature remained at $T = 34.3^\circ$. The resulting intensity distribution can be seen in figure 5.3.

The HFS-spectrum

The etalon is removed for this measurement and the exact same current modulation of the laser current as has been used for the scan-rate measurements will be used here as well. As the intensity increases with increasing diode current, the spectrum would have a linear offset. This can be counteracted by inverting the photo diode signal and adding the diode current signal to it. An additional cosmetic advantage of this is that the peaks are then positive.

5.2 Data analysis

Laser scan rate

In figure 5.3, it has to be noted that the saw-tooth voltage reaches its maximum between the rightmost peak and the one on the left of it, meaning that these two actually belong

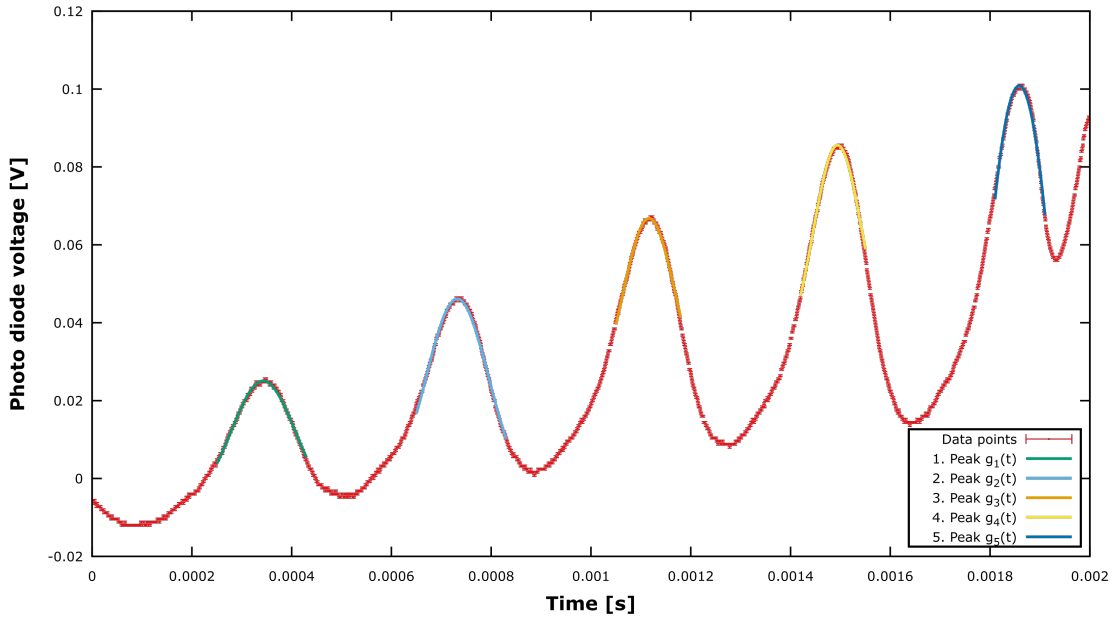


Figure 5.3: Results of the etalon calibration measurements. The rightmost peak is actually the same as the one on the left of it, as the saw-tooth reaches its peak between the two.

to the same frequency. The rightmost peak is thus ignored for the calibration. Gauss functions with a constant offset of the form

$$g_i(t) = a_i * e^{-\frac{(t-t_{0,i})^2}{2*\sigma_i^2}} + c_i \quad (5.1)$$

and a linear offset function $l(t) = b * t + c$ were used. The results for the peak positions $t_{0,i}$ can be seen in figure 5.4. As the linear fit shows, these peaks are equidistant as expected with the time distance between peaks being $b = (0.379 \pm 0.003)$ ms. The nominal distance between two peaks is $\Delta_{FSR} = (9924 \pm 30)$ MHz. With these two values, the scan rate r of the laser can be calculated as

$$r = (26.17 \pm 0.22) \frac{\text{GHz}}{\text{ms}} \quad (5.2)$$

HFS-spectrum

Only 6 of the expected 8 peaks (see fig. 2.2) are visibly separated here. It is reasonable to assume that the peaks that were not separable are those of the transitions ^{85}Rb F:3-2 and ^{85}Rb F:3-3 as well as ^{85}Rb F:2-2 and ^{85}Rb F:2-3. This also means that the hyperfine constant for the $^2S_{1/2}$ of ^{85}Rb cannot be calculated with these measurements. Gauss functions like those in equation 5.1 were used for the individual peaks. However, for the peaks that overlap, as sum of the two functions was used. For all fits, both a linear

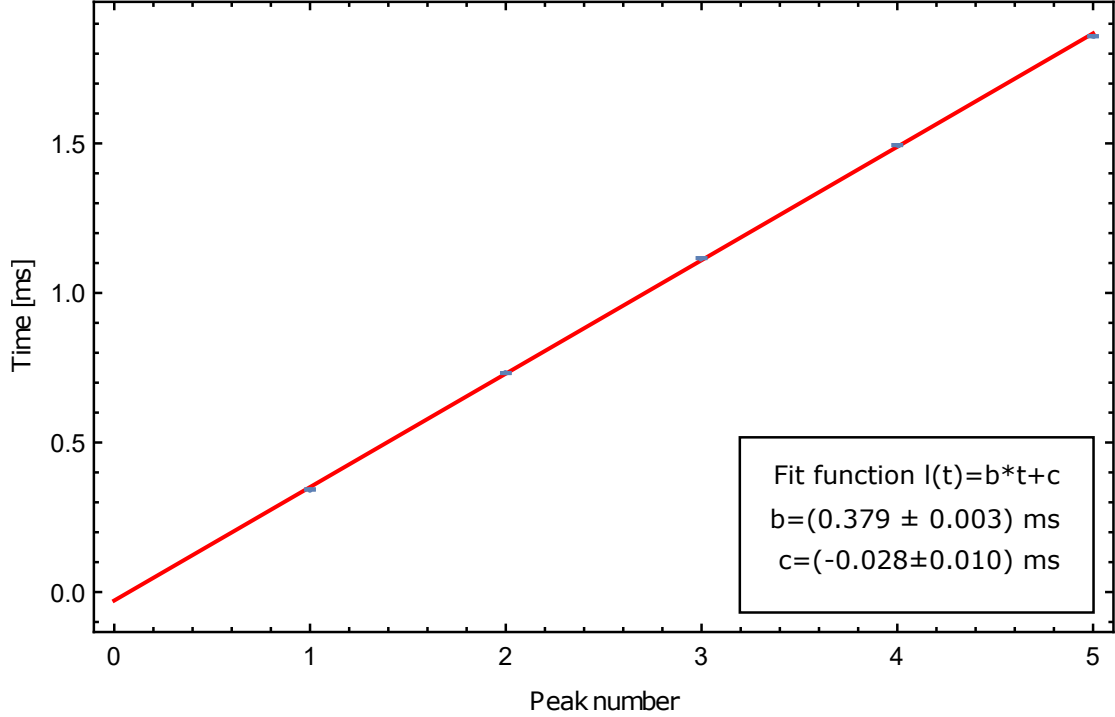


Figure 5.4: Linear fit on the etalon peak positions.

function and a constant were added and the total sum fitted to the data. The fit function for the last three peaks for example was

$$I_{4-6}(t) = g_4(t) + g_5(t) + g_6(t) + b \cdot t + c \quad (5.3)$$

Table 5.1 lists the result of the fits as well as the frequency distances ν_i of the i-th peak to the first peak, which was arbitrarily chosen as a point of comparison. The differences between the peaks were compared to those expected (see fig. 2.2) and the transitions were attributed accordingly. The uncertainties of the peak center times stem from the fits.

With these distances known and the help of equation 2.3, the hyperfine constants can be calculated. For $A_{2P_{1/2}}(^{87}Rb)$, the calculation is

$$A_{2P_{1/2}}(^{87}Rb) = h \cdot \frac{\nu_8 - \nu_7}{F + 1} = (1.52 \pm 0.18) \mu\text{eV} \quad (5.4)$$

where $F = 1$ is the total angular momentum of the atom in the state that the transitions have in common. This value encloses the literature value $A_{2P_{1/2}}(^{87}Rb) = 1.692 \mu\text{eV}$ [4] in its 1σ interval.

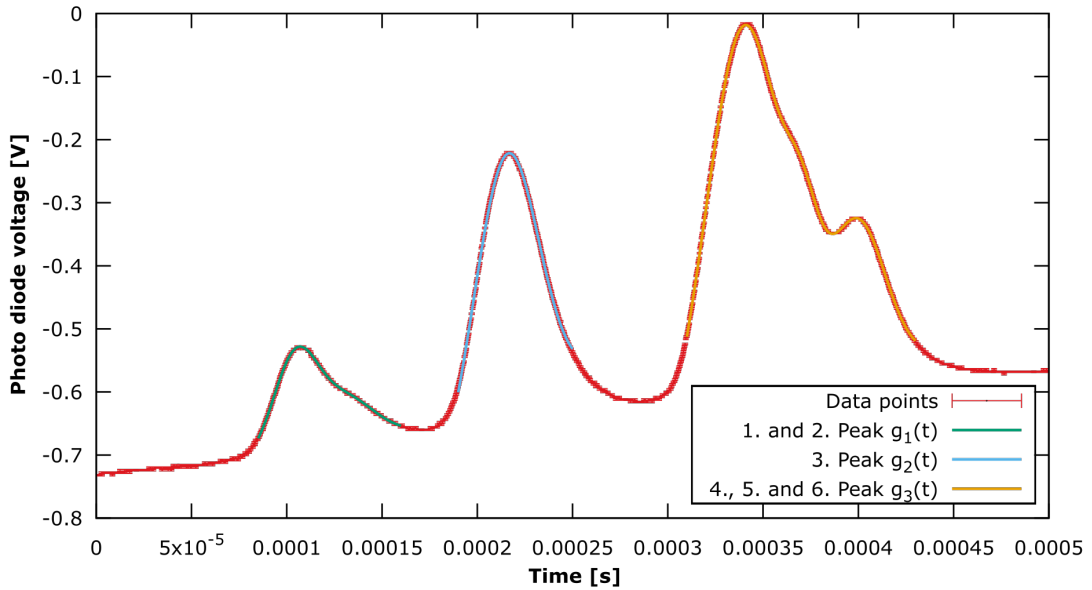


Figure 5.5: The HFS-spectrum with fits to the individual peaks. The signal is negative since it was inverted.

The other two calculable hyperfine constants are

$$A_{2S_{1/2}}(^{87}Rb) = h \cdot \frac{\nu_8 - \nu_2}{F + 1} = (14.61 \pm 0.13) \text{ } \mu\text{eV} \quad (5.5)$$

$$A_{2S_{1/2}}(^{85}Rb) = h \cdot \frac{\nu_{5/6} - \nu_{3/4}}{F + 1} = (4.50 \pm 0.08) \text{ } \mu\text{eV} \quad (5.6)$$

which both place their respective literature values $A_{2S_{1/2}}(^{87}Rb) = 14.13 \text{ } \mu\text{eV}$ and $A_{2S_{1/2}}(^{85}Rb) = 4.185 \text{ } \mu\text{eV}$ outside of their 3σ intervals. While the distance between the first and eighth peak of the spectrum is within 1σ of the expected value, the spectrum in between seems to be somewhat distorted. As we can also not separate the third and forth as well as the fifth and sixth peak, which are both more than 5 times further apart than the largest statistical error that was calculated, one has to assume that either the statistical errors are vastly underestimated or that there is a systematic error that is unaccounted for. Such a systematic error could be a not completely linear current modulation or the effect of the etalon not being placed perfectly perpendicular to the beam.

Peak i	t_0 [ms]	s_{t_0} [μ s]	$\Delta\nu_i$ [GHz]	$s_{\Delta\nu_i}$ [GHz]	$\Delta\nu_i^{theo}$ [GHz]	Transition
1	0.104	0.18	-	-	-	^{87}Rb F:1-2
2	0.129	0.92	0.648	0.005	0.82	^{87}Rb F:1-1
3/4	0.215	0.05	2.905	0.024	2.66 / 3.02	^{85}Rb F:2-2/3
5/6	0.340	0.03	6.17	0.05	5.70 / 6.06	^{85}Rb F:3-2/3
7	0.371	0.06	6.98	0.06	6.83	^{87}Rb F:2-2
8	0.399	0.06	7.71	0.06	7.65	^{87}Rb F:2-1

Table 5.1: Fit results of the Gauss fits on the HFS spectrum. The frequency calibration was used to calculate the frequency differences to the preceding peak. Theoretical values were taken from [1].

6 Double resonance

6.1 Set-up and procedure

This measurement is called double resonance since we both pump the Zeeman states and, at the same time, depopulate the polarized state with radio frequency radiation (RF radiation from here on). Both effects can be described as a resonance. The RF frequency can be measured with a frequency counter which is also built into the glass cell unit. The glass cell is now always lodged in the central unit.

To achieve pumping, the polarization of the laser light needs to be changed from linear to circular. It does not matter where it is right or left circular - that merely changes the direction of polarization. To achieve circular polarization, a quarter wave plate is used. As the polarization after said place depends on the angle of the linear polarization of the incident light, one has to check whether the light is actually circularly polarized after the wave plate. For that, a linear polarizer is used to check whether or not the intensity signal varies upon turning the linear polarizer, which it should not.

A sinusoid current is run through coil 2 (see fig. 6.1), at first with a large amplitude to find the magnetic field range for which double resonance occurs. Once the range is determined, a constant current is applied to coil 1. The double resonance peaks are now visible, but Dehmelt peaks, which are a result of relaxation once the magnetic field crosses zero, are still visible. It can easily be determined which is which, as the double resonance peaks disappear when one turns off the RF generator. For the Dehmelt peaks to disappear, the amplitude of the sinusoid in current two has to be reduced so that the overall magnetic field does not cross zero anymore. Coil 4, which creates a field along the x-axis in figure 6.1, can now be used to compensate the vertical magnetic field of the earth. When it is compensated, the negative peaks should have maximal depths. The current through coil 4 is then kept at this value for the main measurement.

With the vertical magnetic field compensated, the current in coil 1 can now be tuned to make the two peaks per period equidistant. In this state, the magnetic field from coil 1 stretches the Zeeman spectrum exactly enough for the RF frequency to relax the

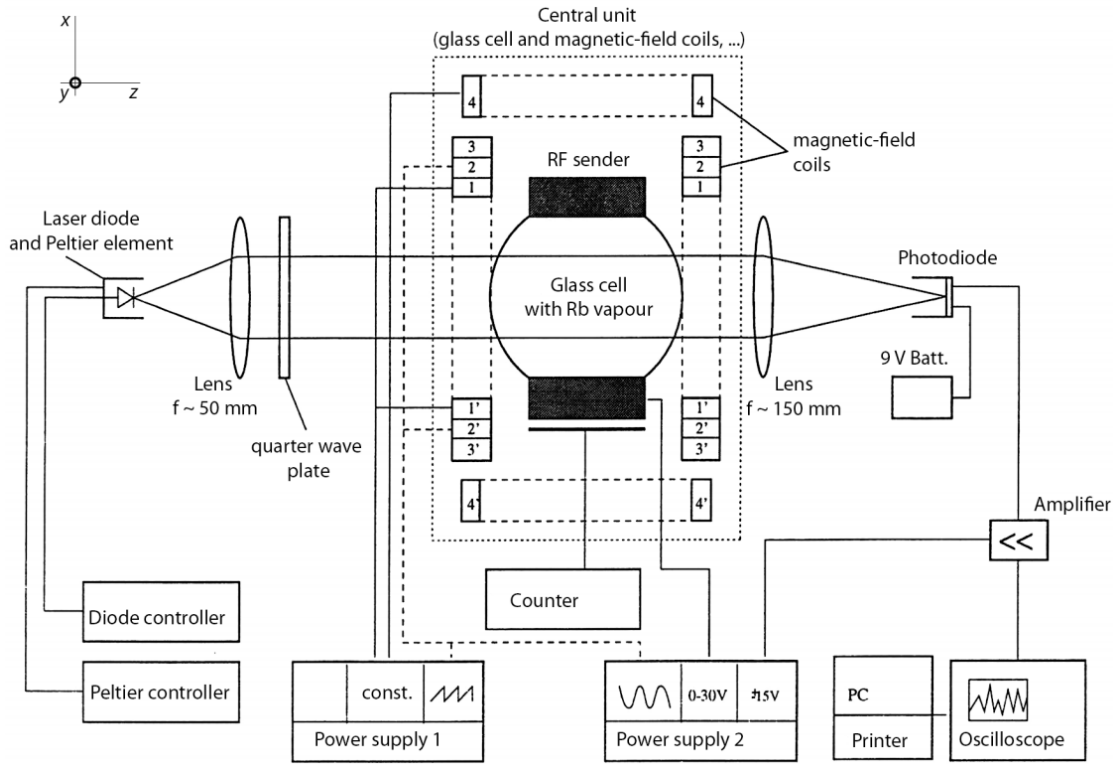


Figure 6.1: Experimental set-up for the double resonance measurements.[2]

polarization. One such value must exist for both current directions through coil 1. This is done for both rubidium isotopes. The laser current is measured with an exterior multimeter, since the digital display has a precision of 1 mA. From these four values, the longitudinal magnetic field of the earth can be measured and the nuclear spins I of the isotopes calculated.

6.2 Data analysis

Measurements were taken at $T = 34.4^\circ$ and with a RF frequency of $\nu_{RF} = (497 \pm 1) \cdot 10^3$ Hz. An uncertainty of $s_{I_{C1}} = 0.5$ mA was estimated for current at which the peaks are equidistant. The results can be seen in table 6.2. The current in coil 4 for which the vertical field was compensated was determined to be $I_{C4} = (78 \pm 3)$ mA.

The constants $c_B = B/I$ of the coils in table 6.1 were provided for the calculations of the magnetic fields that the coils create.

The magnetic fields are

$$B = c_b \cdot I_C, \quad s_B = \sqrt{(c_b \cdot s_{I_C})^2 + (I_C \cdot s_{c_b})^2} \quad (6.1)$$

where I_C is the current in the respective coil. Table 6.2 lists those results for coil 1. From

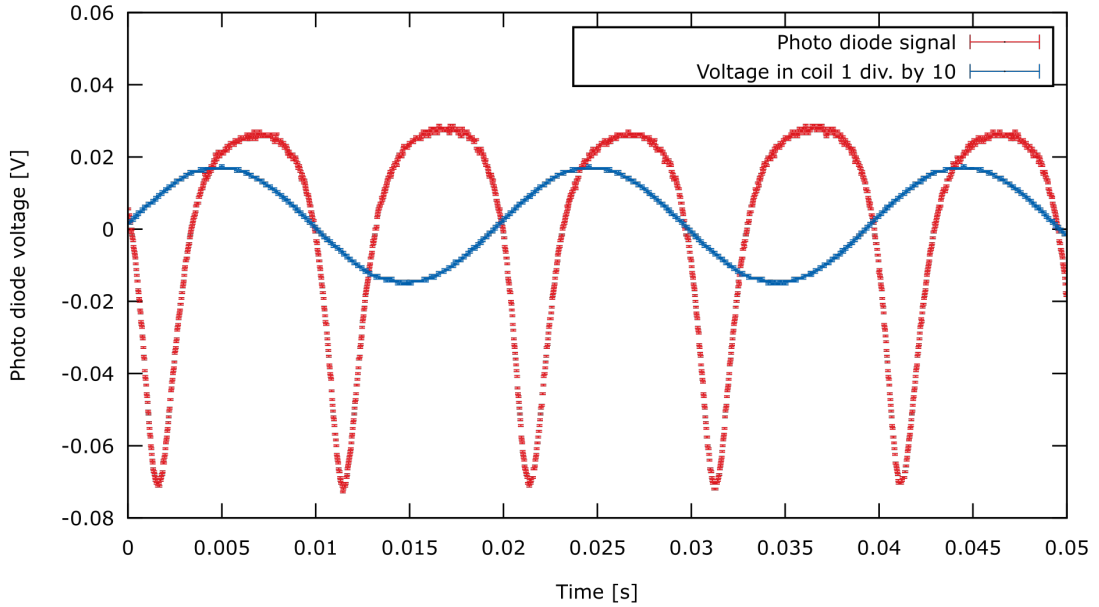


Figure 6.2: Equidistant peaks for $I_L = 61.8$ mA and a current in coil 1 of $I_{C1} = 130.2$ mA. Note the phase shift: The double resonance peaks do not occur at the zero-crossing of the coil voltage, but at those of the coil current. The coil voltage was divided by ten to make the photo diode signal more dominant.

Coil No	n	d [m]	calc. B/I [$\frac{\text{Vs}}{\text{Am}^2}$]	meas. B/I [$\frac{\text{Vs}}{\text{Am}^2}$]
1	80	0.09	$8.0 \cdot 10^{-4}$	$7.99(1) \cdot 10^{-4}$
2	80	0.09	$8.0 \cdot 10^{-4}$	$8.14(1) \cdot 10^{-4}$
3	16	0.09	$1.7 \cdot 10^{-4}$	–
4	60	0.246	$4.4 \cdot 10^{-4}$	$4.76(1) \cdot 10^{-4}$

Table 6.1: The B/I values and properties of the Helmholtz coils. n is the number of windings. [2]

I_L [mA]	s_{I_L} [mA]	I_{C1} [mA]	$s_{I_{C1}}$ [mA]	B_{C1} [μT]	$s_{B_{C1}}$ [μT]
62.4	0.1	91.2	0.5	71	10
62.4	0.1	-85.3	0.5	85	9
61.8	0.1	136.1	0.5	109	12
61.8	0.1	-130.2	0.5	104	11

Table 6.2: The results of the double resonance measurements. The magnetic field signs were matched with those of the currents.

the current in coil 4, the vertical magnetic field was calculated to be

$$B_v = (37.1 \pm 1.4) \mu\text{T} \quad (6.2)$$

The magnetic fields are all written with positive sign. Let B_1 be the magnetic field of the positive, B'_1 the negative coil current. The horizontal component of the earth's magnetic field is equal to half the difference of these two fields

$$B_h = \frac{B_1 - B'_1}{2}, \quad s_{B_h} = \frac{1}{2} \cdot \sqrt{s_{B_1}^2 + s_{B'_1}^2} \quad (6.3)$$

The magnetic field difference is identical for the two isotopes, but the error is slightly different. The mean of the two is

$$B_h = (2.36 \pm 0.21) \mu\text{T} \quad (6.4)$$

When calculating the mean value of B_1 and B'_1 ,

$$\bar{B}_1 = \frac{B_1 + B'_1}{2} \quad (6.5)$$

the magnetic field component of the earth cancels out and yields the magnetic field that is responsible for the Zeeman splitting. Together with the frequency ν_{RF} and by using equation 2.4, the nuclear spins I of the two isotopes can be calculated as

$$I = \frac{\mu_B \cdot \bar{B}_1}{h \cdot \nu} - \frac{1}{2}, \quad s_I = \frac{\mu_B \cdot \bar{B}_1}{h \cdot \mu} \sqrt{\left(\frac{s_{\bar{B}_1}}{\bar{B}_1}\right)^2 + \left(\frac{s_\nu}{\nu}\right)^2} \quad (6.6)$$

Since greater diode current corresponds to lower frequency and thus lower transition energy, the current $I_{C1} = 62.4(1)$ mA corresponds to ^{87}Rb and the $I_{C1} = 61.8(1)$ mA to ^{85}Rb . The results for the spins were

$$I(^{85}\text{Rb}) = 2.496 \pm 0.009 \quad (6.7)$$

$$I(^{87}\text{Rb}) = 1.486 \pm 0.007 \quad (6.8)$$

$$(6.9)$$

6.3 Discussion

The literature values for the earths' magnetic field are [2]

$$B_v^{lit} = 42.9 \text{ } \mu\text{T}, \quad B_h^{lit} = 20.9 \text{ } \mu\text{T} \quad (6.10)$$

while the measurements yielded $B_h = (2.36 \pm 0.21) \text{ } \mu\text{T}$ and $B_v = (37.1 \pm 1.4) \text{ } \mu\text{T}$. While the result for the vertical field encloses the literature value in its 4σ interval, the result for the horizontal field is nowhere near the expected value. To double check the results, a Hall effect sensor was used. Since the sensor only had a resolution of $10 \text{ } \mu\text{T}$, it only useful for qualitative analysis. These measurements revealed that not only is the horizontal field much weaker inside the metal casing of the experimental set-up, the experimental set-up is also not aligned with the projection of the magnetic field lines on its horizontal axis. Due to time constraints, the measurements could not be repeated with an aligned table. The deviation in the vertical field can likely be attributed to shielding effects of the building.

The calculated values for the spins are in good agreement, enclosing the expected values of $I(^{87}) = 3/2$ in the 2σ interval and $I(^{85}) = 5/2$ in the 1σ interval.

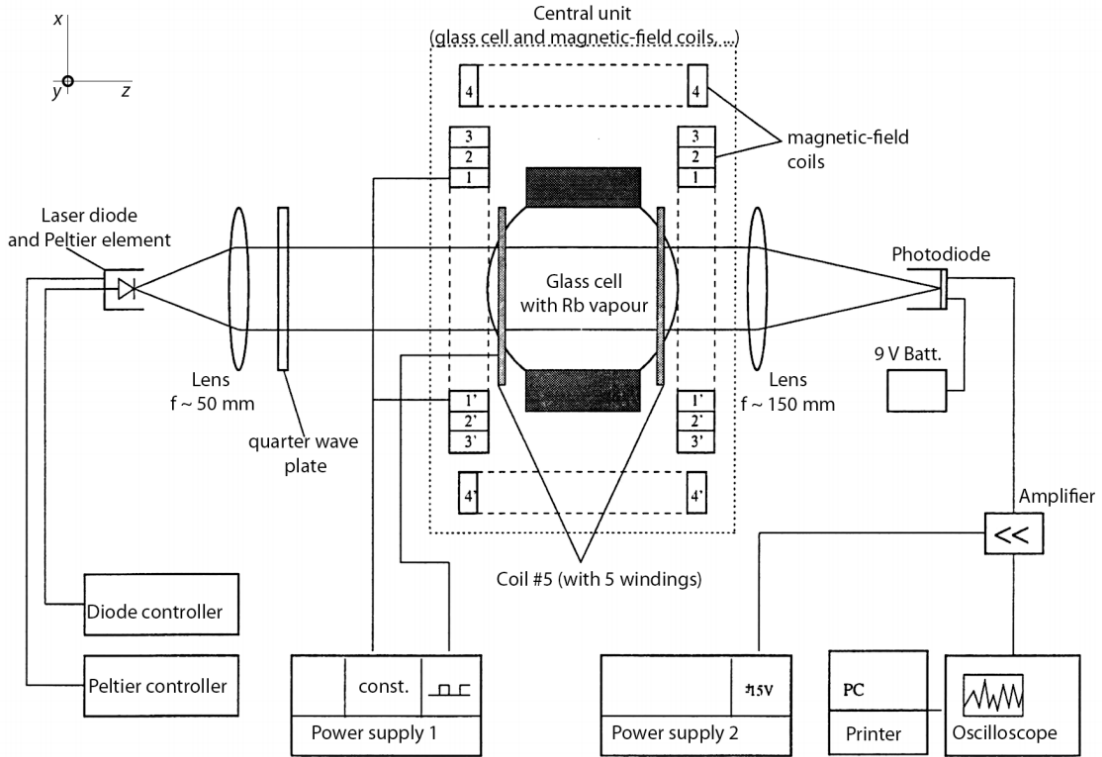


Figure 7.1: Experimental set-up for the spin precession measurements. [2]

7 Spin precession

7.1 Set-up and procedure

As before, only a quarter wave plate and the glass cell are placed in the beam. For the spin precession, the horizontal field as it was calculated in the double resonance section is compensated with a current in coil 1. A rectangular signal is given onto coil 5 so that the horizontal component of the magnetic field is compensated regularly. The spin precedes around the remaining vertical component, which can be varied by currents in coil 4. Measurements of the precession are then taken for a range of currents in coil 4.

Upon initial measurements, where both horizontal and vertical component were compensated as per the results from the double resonance section, it became clear that there was still a magnetic field, since precession could still be observed. As mentioned before, the table is not aligned with the horizontal component of the earth's magnetic field. Thus, the table was rotated until a minimal precession frequency was found. The degree by which the table was turned was by $\phi = (7 \pm 2)^\circ$ and measurements were then taken as described above.

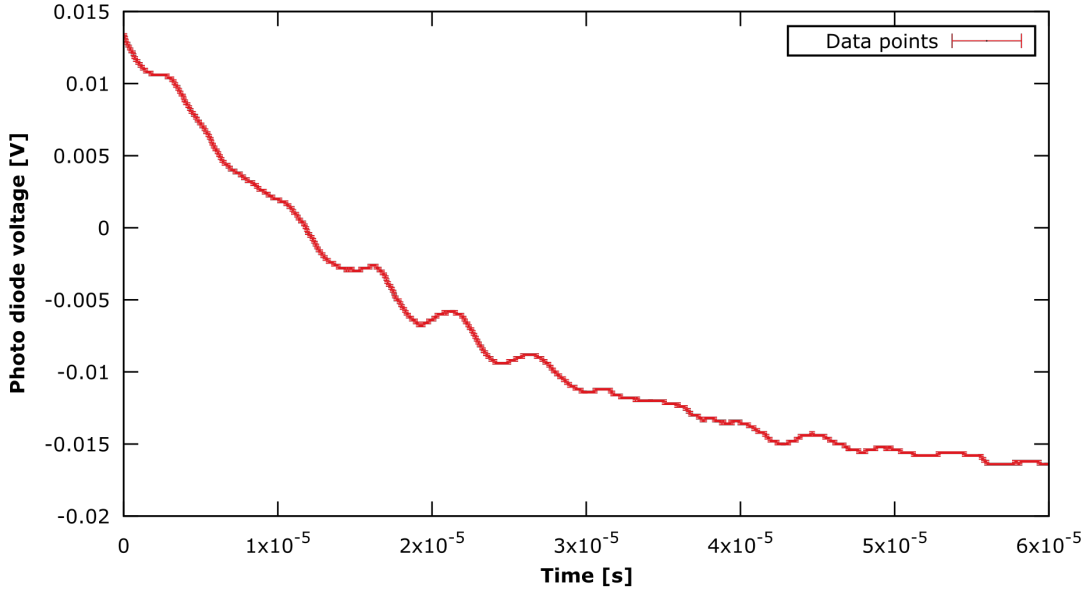


Figure 7.2: Exemplary plot of the spin precession measurement. The peak positions were read off.

7.2 Analysis

Measurements were taken only for a diode current of $I_L = 62.0$ mA, which was the current corresponding to ^{87}Rb . No precession signal was found for ^{85}Rb . The temperature during the measurements was $T = 34.3^\circ$ and the current for the compensation of the horizontal field after turning the table was $I_{C1} = (6 \pm 1)$ mA.

The time differences between peaks were read out of appropriate sub plots of the recorded data. One exemplary plot can be seen in figure 7.2 and all the values that were read out in table 7.1. First, the time difference Δt and its error were calculated

$$\Delta t = t_2 - t_1, \quad s_{\Delta t} = \sqrt{2} \cdot s_{t_{12}} \quad (7.1)$$

where $s_{t_{12}}$ is the estimated error on reading the peaks as it is listed in table 7.1.

There sometimes were no properly readable adjacent peaks. While it was always clear that there was a peak, it was much easier to read out the second most adjacent peak. Those values are marked with a star in the first column in table 7.1 and their time difference is

$$\Delta t = \frac{t_2 - t_1}{2}, \quad s_{\Delta t} = \frac{1}{\sqrt{2}} s_{t_{12}} \quad (7.2)$$

The precession frequency ν_L can now be calculated

$$\nu_L = \frac{1}{\Delta t}, \quad s_{\nu_L} = \frac{s_{\Delta t}}{(\Delta t)^2} \quad (7.3)$$

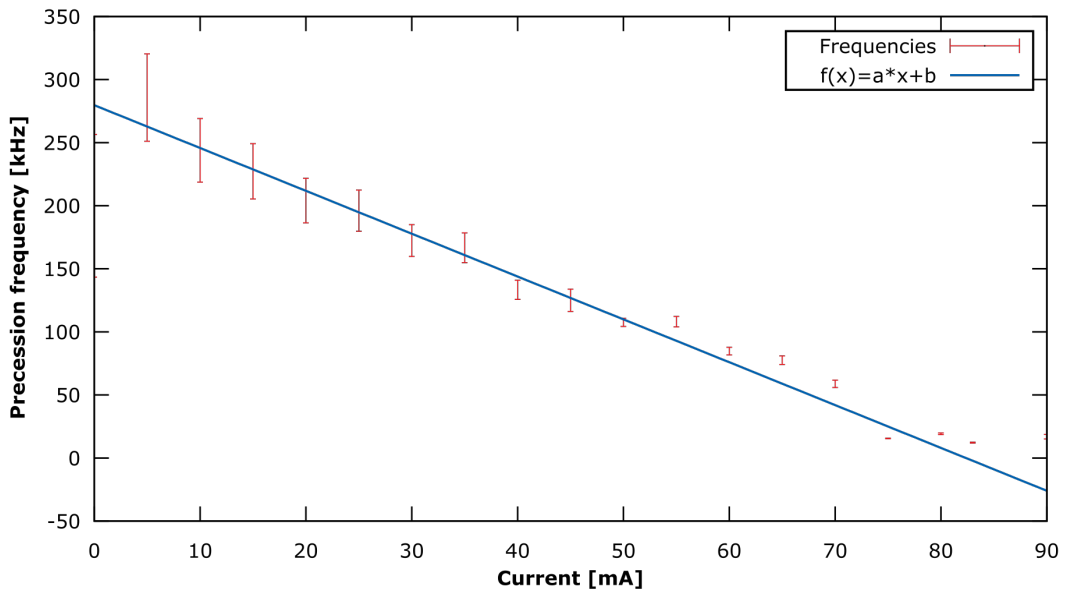


Figure 7.3: The precession frequencies and the according linear fit. The x-axis cut can be calculated from the fit parameters and represents the current in coil 4 for which the vertical magnetic field is fully compensated.

and the results are plotted in figure 7.3. A linear fit $f(x) = a \cdot x + b$ was used to describe the data and the resulting parameters were $a = (-3.40 \pm 0.17)$ kHz/mA and $b = (280 \pm 11)$ kHz with $\chi^2 = 9.9$. One can extrapolate to the magnetic field for which the precession frequency would be zero, assuming that all other fields were actually compensated for. The current in coil 4 for said field is $I_{C4}^0 = \frac{-b}{a} = (82 \pm 5)$ mA and the according magnetic field $B_v = 39.2 \pm 2.5$ μT . This is within 1σ of the value calculated in the double resonance section.

Since the magnetic field is reduced until it reaches above field, the negative value of the fit constant a corresponds to the proportionality constant $\alpha_{lit} = 6.998$ kHz/ μT between the magnetic field and the precession frequency as it was defined in 2.11. It is however still given in kHz/mA and needs to be translated to kHz/ μT to be comparable. The result is

$$\alpha = \frac{a}{c_b} (7.1 \pm 0.4) \text{ kHz}/\mu\text{T} \quad (7.4)$$

where $c_b = 0.476(1)$ $\mu\text{T}/\text{mA}$ is the proportionality factor between current and magnetic field for coil 4. This value includes the literature value in its 1σ interval.

I_{C4} [mA]	t_1 [10^{-5} s]	t_1 [10^{-5} s]	$s_{t_{12}}$ [10^{-5} s]
0	2.0	2.5	0.1
5	1.85	2.20	0.03
10	2.01	2.42	0.03
15	1.74	2.18	0.03
20	1.93	2.42	0.03
25	2.12	2.63	0.03
30	1.80	2.38	0.03
35	2.08	2.68	0.03
40	4.25	5.00	0.03
45*	4.52	5.32	0.04
50*	5.37	7.23	0.04
55*	5.38	7.23	0.05
60*	4.74	7.10	0.06
65*	5.45	8.03	0.08
70*	14.4	17.8	0.12
75	16.5	29.4	0.12
80	15.0	20.2	0.13
83	19.6	27.8	0.18
90	21.9	27.8	0.45

Table 7.1: The B/I values and properties of the Helmholtz coils. n is the number of windings. [2]

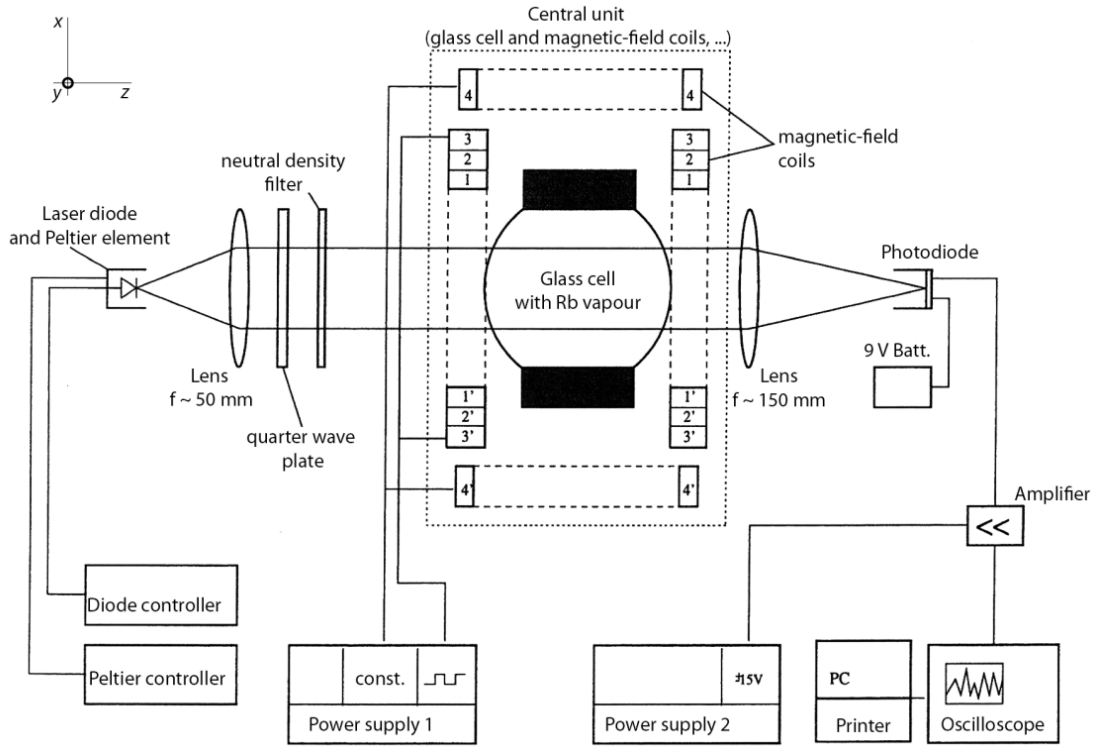


Figure 8.1: Set-up for the relaxation measurements with the Dehmelt method. A range of neutral filter was used. [2]

8 Relaxation measurements - Dehmelt method

8.1 Set-up and procedure

If the ^{87}Rb atom were in a pumped state, say $F = 2$ and $m_F = 2$ for example, and the magnetic field responsible for the Zeeman splitting is suddenly reversed, the system is then pumped into the state $F = 2, m_F = -2$. The measured intensity, after dropping sharply upon reversing the field, increases exponentially until the system is fully pumped. The speed of this process depends both on the laser intensity and speed of relaxation. If one measures this process for various laser intensities, facilitated with neutral filter (see fig. 8.1), the relaxation time T_R of the system can be extracted as it remains constant. For these measurements, the vertical magnetic field will be compensated by coil 4 while coil 3 induces the reversing magnetic field.

8.2 Data Analysis

All measurements were taken at $T = 34.3^\circ$ and a laser current of $I_L = 61.6 \text{ mA}$. As the actual intensity reduction capabilities of the filter were unknown, a calibration measurement of all filters that are later to be used was done. First, a measurement of

Filter name	I_L [V]	I_{rel} [%]	$s_{I_{rel}}$ [%]	τ [ms]	s_τ [ms]
No filter	1.40	100.0	0.8	0.437	0.002
Triangle	1.11	80.1	0.7	0.503	0.002
Circle	0.68	50.8	0.6	0.712	0.002
-0,37	0.55	42.0	0.5	0.859	0.002
D0,3	0.50	38.5	0.5	0.842	0.002
0,6	0.48	37.4	0.5	1.121	0.05
D0,6	0.41	32.2	0.5	0.995	0.005
D1,0	0.39	31.2	0.5	1.574	0.008
-0,8	0.17	15.8	0.6	1.602	0.007
-1,03	0.16	15.2	0.6	2.048	0.023
D1,3	0.07	8.8	0.6	1.975	0.024
No laser	-0.06	0.0	0.6	-	-

Table 8.1: The relative intensities for the neutral filters. Measurements were only possible for filter until the one marked D1,3.

the intensity without any filter I_{NF} and one of the intensity signal with the laser turned off I_0 were taken. The relative intensity of the former is then set as 1, the one of the latter as 0. The relative intensities for the filter I_F^{rel} are calculated from their absolute measured intensities I_F as

$$I_F^{rel} = \frac{I_F - I_0}{I_{NF} - I_0} \quad (8.1)$$

Table 8.1 shows the results of these calculations. The errors were calculated through Gaussian error propagation.

When available, the classification of the filter was used as a name. However, the filter named *triangle* and *circle* did not have a classification written on them, but instead the aforementioned symbols.

For these filters, measurements of the relaxation time were taken. One such example can be seen in figure 8.2. Equation 2.9 suggests using an exponential fit to describe the data:

$$I(t) = I_{max} - \Delta I \cdot e^{-a \cdot (t-t_0)} \quad (8.2)$$

where I_{max} is the intensity in the pumped state, ΔI the amplitude of the change in intensity and t_0 is an offset on the time axis to adjust for the fact that the magnetic field was not inverted at $t = 0$. The deciding parameter however is $a = 1/\tau$, the inverse of the orientation time of the system. The respective values for τ are listed in table 8.1. The values for a can now be plotted against the relative intensities of the filter they were measured with. The result can be seen in figure 8.3. Equation 2.10 and the fact the the

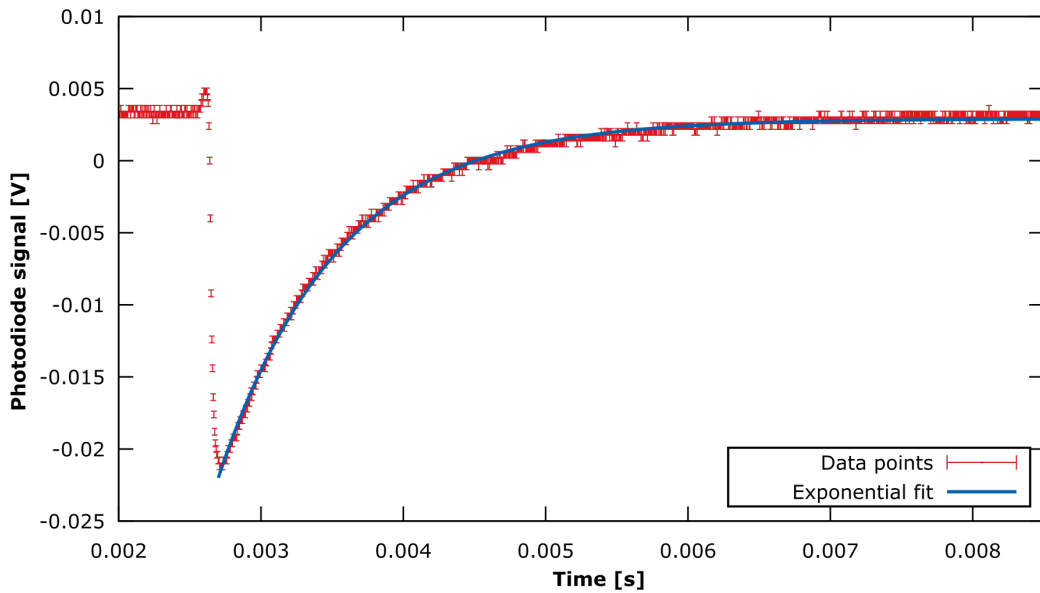


Figure 8.2: Relaxation data recorded with the neutral filter D0,3.

pumping time is inversely proportional to the intensity, $T_P = \frac{1}{\alpha I}$, calls for a fit of the form

$$a(I_{rel}) = \alpha I_{rel} + \frac{1}{T_R} \quad (8.3)$$

The values are far more scattered than the uncertainties would suggest. This is expressed in a large $\chi^2 \approx 105$ as well as in a large error in the desired variable $T_R = (4.8 \pm 1.5)$ ms. Due to this large error, it includes the expected result of $T_R^{lit} = 6.5$ ms in its 2σ interval. One likely reason for the larger than expected fluctuation in inverse orientation times would be temperature fluctuations. These have a strong effect on the laser intensity. In the theoretically calculated value, the spin-spin exchange was not taken into account and many calculations were simplified. This might also explain why the measured relaxation time is smaller than predicted.

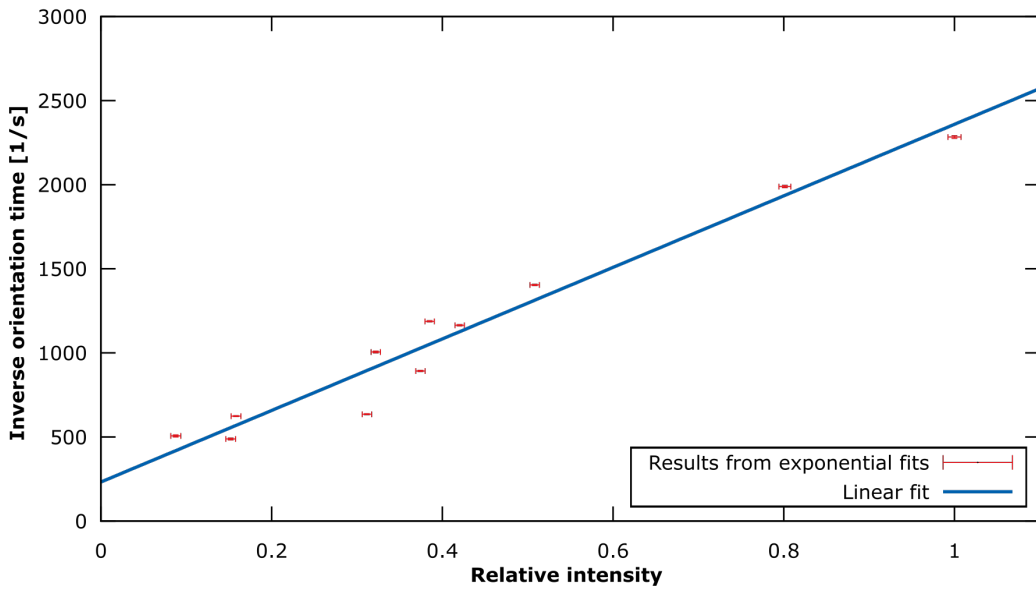


Figure 8.3: The fit parameter a , which is the inverse orientation time, plotted for the respective relative intensity.

9 Relaxation measurements - Franzen method

9.1 Set-up and procedure

The Franzen method of determining the relaxation time relies on completely blocking and transmitting the laser. During the time when the laser is blocked ("darkness"), the system relaxes and, once the laser is transmitted again, causes exponentially dissipating absorption. The value from which the absorption reduces exponentially depends on the time for which the system was in darkness. The periodic blocking of the laser is facilitated by the chopper disk, which is placed as close to the laser as possible to make the cutting process faster. The laser current is set to maximize absorption signals.

9.2 Data Analysis

Measurements were taken at $T = 34.3^\circ$ and $I_L = 60.4$ mA. The vertical component of the earth's magnetic field remains compensated. For very low chopper voltages, the chopper signal was unstable and it was concluded that the motor does not operate steadily for such voltages. Measurements were then taken for motor voltages between 4 V and value unit. The results of one such measurement can be seen in figure For the fits, a Fermi function with a constant offset was used to approximate the intensity modulation by the chopper

$$I_{Ch}(t) = \frac{A}{1 + e^{\frac{\mu - x}{\sigma}}} + U \quad (9.1)$$

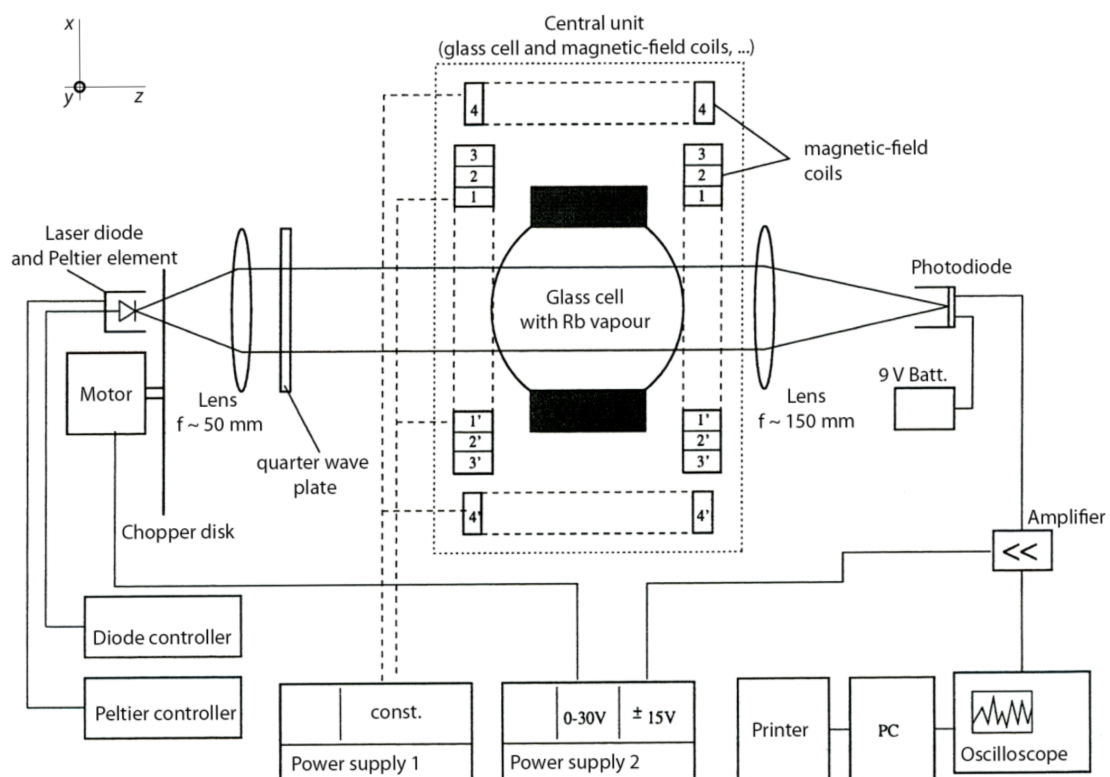


Figure 9.1: Set-up for the relaxation measurements with the Franzen method. The laser beam is periodically blocked with the chopper.[2]

The relaxation, described by an exponential function, was made to start as soon as the Fermi function reaches 1% intensity, which is true for $x > \mu - \sigma \log(99)$:

$$I_R(t) = \begin{cases} 0 & t \leq \mu - \sigma \log(99) \\ B \cdot (1 - e^{-\lambda(t-\mu)}) & t \geq \mu - \sigma \log(99) \end{cases} \quad (9.2)$$

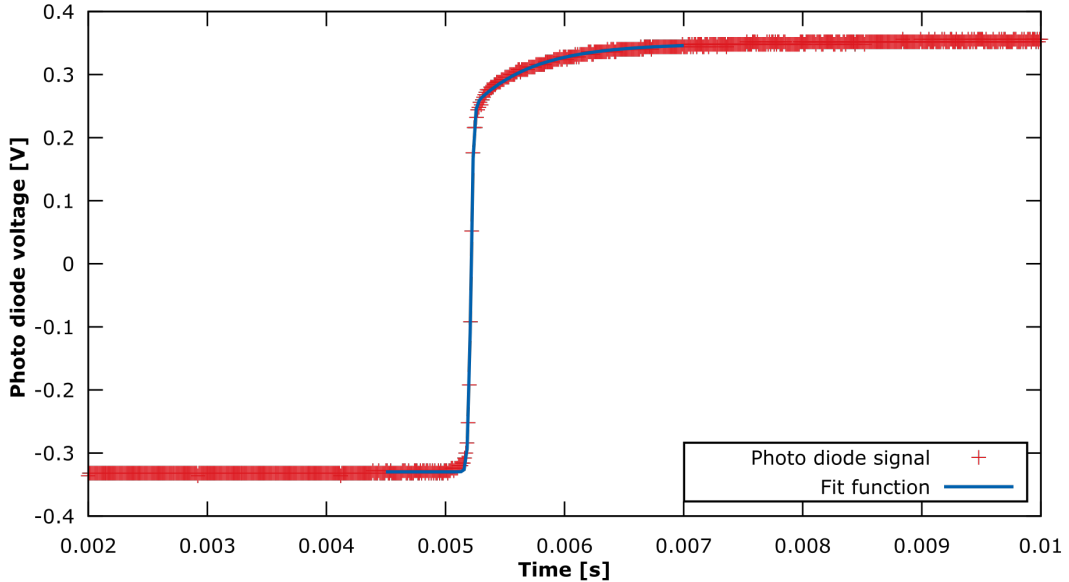


Figure 9.2: The relaxation measurement for a chopper voltage of 4 V and the according fit.

These fits were very sensible to the starting parameters. The parameter B is the absorption at $t = \mu - \sigma \log(99)$ and thus the sought after parameter. The dark times t_d were taken from the data by hand and an uncertainty estimated each time. The parameter B for the different dark times can be seen in figure 9.3. A fit of the form

$$B(t_d) = a + b \cdot (1 - e^{-\frac{t_d}{T_R}}) \quad (9.3)$$

where a is an offset and b is the amount of relaxation for large t_d . The data however is very linear and the fit thus converges only for very large T_R . The result for the relaxation time was

$$T_R = (50 \pm 24 \cdot 10^5) \text{ s} \quad (9.4)$$

Not only is the error astronomically large, the value is also several orders of magnitude away from the expected value of $T_R^{lit} = 6.5 \text{ ms}$. Longer dark times would likely have been needed for better measurements, but as mentioned before, the motor was not completely

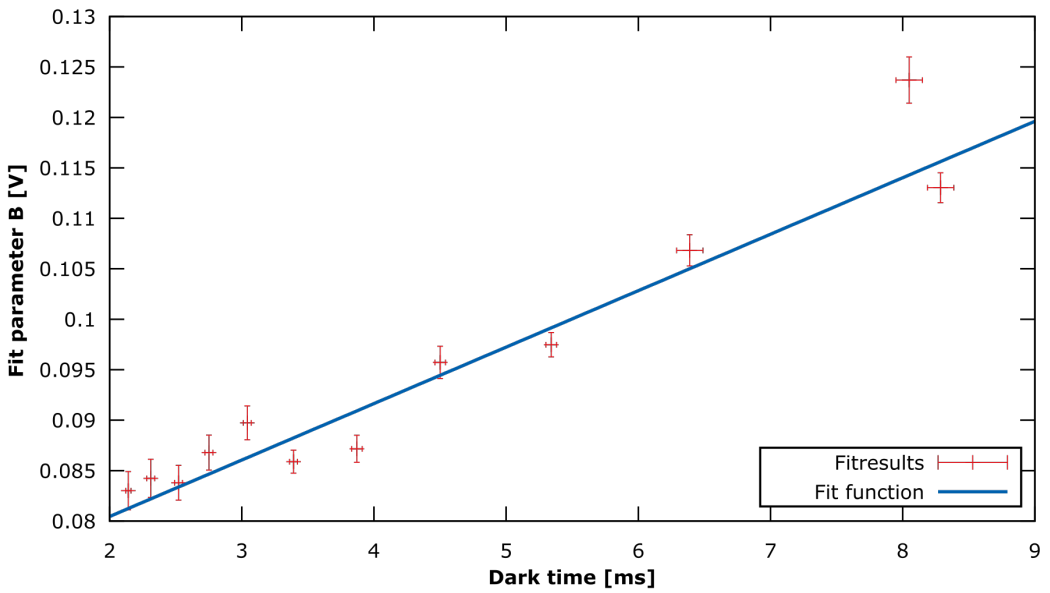


Figure 9.3: The calculated fit parameters B for the respective dark times.

reliable for voltages below 3 V. Figure 9.4 shows the signal for 1.5 V. The time that the edge of one opening in the chopper takes to fully pass by the laser is roughly 0.5 ms and thus a significant time compared to the expected relaxation time of 6.5 ms. Furthermore, the dark and light times seemed rather inconsistent, suggesting that the motor maybe does not operate at a constant speed.

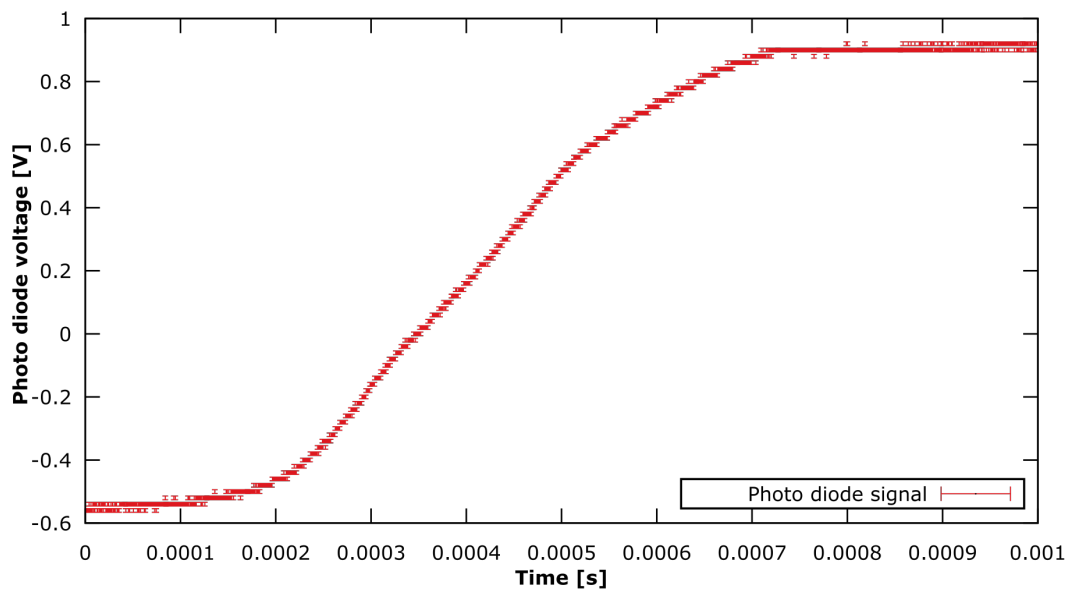


Figure 9.4: The chopper signal for a supply voltage of 1.5 V. The chopper takes roughly 0.5 ms to fully pass by the laser. This is a significant time for the measurement period.

10 References

- [1] Baur, Clemens. *Einrichtung des Versuchs "Optisches Pumpen mit Laserdioden"*. Zulassungsarbeit. Freiburg 1997
- [2] *Instructions for the experiment "Optical Pumping"*. Albert-Ludwig University Freiburg. Freiburg 02.2016
- [3] Happer, William. *Optical pumping*. *Reviews of Modern Physics* 44.2 (Apr. 1972): 170-238
- [4] Corney, A. *Atomic and Laser Spectroscopy*. Oxford University Press, 1977